Magnesium Technology 2011
Edited by: Wim H. Sillekens, Sean R. Agnew, Neale R. Neelameggham, and Suveen N. Mathaudhu
TMS (The Minerals, Metals & Materials Society), 2011

Dendritic Microstructure in Directional Solidification of Magnesium Alloys

Morteza Amoorezaei, Sebastian Gurevich, Nikolas Provatas

Department of Materials Science and Engineering, McMaster University, 1280 Main Street West; Hamilton, Ontario, L8S4L7, Canada

Keywords: directional solidification, magnesium, dendrite, transition

Abstract

We demonstrate morphological transitions in Mg-Al alloy dendritic microstructure as the cooling conditions change during steady state and transient directional solidification. The effect of temperature gradient on the transition is investigated numerically using two-dimensional phase field simulations. The six-fold symmetry of Mg alloys leads to very different dendrite morphologies than those encountered in alloys exhibiting four-fold surface tension anisotropy. In particular, we find that at high temperature gradients primary dendrites become columnar in the direction of thermal gradient. In contrast, in the regions where surface energy anisotropy is dominant, primary stalks cross at 60-degree angles that characterize hexagonal crystal structure. Our modelling observations are compared to new Mg-Al experiments.

Introduction

Predicting and controlling the as-cast microstructure during solidification of alloys is crucial to obtain desired properties. Specifically in emerging technologies such as strip casting, where few thermomechanical processes are applied, the microstructure established at the time of solidification strongly correlates with the mechanical properties of the alloy.

Columnar dendritic arrays are an important class of solidification microstructures that have been studied through directional solidification, where the temperature gradient is established in the direction that heat is extracted while the temperature is essentially uniform in the transverse direction. Directional solidification experiments are carried out under constant (Bridgeman-type) or transient (industrial-type) growth conditions. Industrial experiments usually occur under transient growth conditions where front velocity (V) and temperature gradient (G) are coupled. In contrast, V and G can independently vary in Bridgeman-type directional solidification.

Columnar dendritic microstructure has mostly been studied in alloys with cubic crystal structure [1, 2, 3, 4], where their four-fold symmetry allows studying the dynamical spacing selection between dendrites as the growth conditions vary dynamically. However, very little is known about dendritic microstructure of alloys with hexagonal crystal structure such as Mg-based alloys. Mg is gaining importance in transportation industries due to the high strength-weight ratio, which accordingly leads to lower fuel consumption in the transportation sector. The six-fold symmetry of these alloys induces a competition over growth direction between the anisotropy of surface energy and temperature gradient imposed by the external heat flux. This leads to various dendritic morphologies as the growth conditions and orientation change, which consequently introduces a transition from anisotropy-dominant to temperature gradient-dominant microstructure.

In this paper we investigate the anisotropy-heat flux competition in Mg-Al alloys directionally solidified under transient conditions relevant to industrial applications. We present new 2-D phase field simulations implemented on an adaptive mesh scheme. For brevity, we present simulations for a single grain where interaction between the grains is neglected. Our multigrain simulations and more qualitative studies on the morphological transition will be presented in upcoming publications.

Methods

Experimental Procedure

As received Mg-0.5$wt\%Al$ alloys were employed in this study. Upward transient directional solidification was achieved utilizing a cylindrical stainless steel crucible being water jet cooled from below. To prevent heat extraction from the walls, the crucible was shielded by cylindrical alumina insulation with a thickness of about 10 mm. To measure the temperature at different height

of the melt, twelve K-type thermocouples were aligned at the centre of the crucible 1 mm separated from each other and starting at 1 mm from the chilling surface. More details about the experimental set up are found in [1]. We applied air and water with different pressures as the coolant to obtain a wide range of cooling rates. The obtained temperature gradient at liquidus temperature covered the range of 0.6 to 4.45 K/mm and the growth velocity varied from 0.43 to 3.7 mm/sec.

To reveal the microstructure, the specimens were polished down to 0.05 μm and etched in a solution of 20-ml Water, 20-ml acetic acid, 60-ml ethylene glycol and 1-ml HNO_3 for about 5 minutes.

Phase field method

We consider unidirectional solidification of Mg-$0.5wt\%Al$. In the dilute limit, the solidus and liquidus lines can be approximated by straight lines of slopes m/k and m, respectively, leading to the partition relation $c_s = kc_l$, where c_s (c_l) is the concentration of impurities at the solid (liquid) side of the interface, and k is the partition coefficient. The simulations are two-dimensional, corresponding to a longitudinal section through a row of dendrites coinciding with the basal plane. Given that thermal diffusion is orders of magnitude faster than solute diffusion, latent heat production is neglected, resulting in the frozen temperature approximation $T(z,t) = T_0 + G(t)(z - z_0 - \int_0^t V_p(t')dt')$, where $T(z_0,0) = T_0$ is a reference temperature, while $G(t)$ and $V_p(t)$ are the local thermal gradient and pulling speed, respectively. Fixing the reference concentration as the impurity concentration on the liquid side of an advancing steady-state planar interface $c_l^0 = c_0/k$, where c_0 is the nominal alloy composition, we obtain the following sharp interface solidification equations:

$$\partial_t c = D\nabla^2 c \qquad (1)$$

$$c_l(1-k)v_n = -D\partial_n c|_l \qquad (2)$$

$$c_l/c_l^0 = 1 - (1-k)\kappa d_0\gamma(\theta)$$

$$-(1-k)\left(z - \int_0^t V_p(t')dt'\right)/l_T - (1-k)\beta v_n \qquad (3)$$

where $d_0 = \Gamma/\Delta T_0$ is the solutal capillary length, $\Delta T_0 = |m|(1-k)c_l^0$ the freezing range, $\gamma(\theta)$ the orientation dependent interface stiffness according to the underlying crystalline structure, $l_T = \Delta T_0/G$ the thermal length, D the diffusivity of solute in the liquid, and $\beta = 1/(\mu_k \Delta T_0)$ the kinetic coefficient.

Our phase-field formulation of equations (1)-(3) is based on the model developed by Karma and co-workers and detailed extensively elsewhere [5, 6]. The corresponding evolution equations are given in terms of a generalization of the field $\tilde{U} = (c - c_l^0)/(c_l^0(1-k))$, which represents the local supersaturation with respect to the point (c_l^0, T_0):

$$U = \frac{1}{1-k}\left(\frac{c/c_l^0}{(1-\phi)/2 + k(1+\phi)/2} - 1\right) \qquad (4)$$

with the phase-field variable valued at $\phi = 1$ (-1) in the solid (liquid). Their explicit form is given by:

$$\tau(\hat{n})\left(1 - (1-k)\frac{(z - z_{\rm int})}{l_T}\right)\frac{\partial\phi}{\partial t} = w_0^2\vec{\nabla}\left[a(\hat{n})^2\vec{\nabla}\phi\right]$$

$$+\phi - \phi^3 - \lambda(1-\phi^2)^2\left(U + \frac{z - z_{\rm int}}{l_T}\right) \qquad (5)$$

$$\left(\frac{1+k}{2} - \frac{1-k}{2}\phi\right)\frac{\partial U}{\partial t} = \vec{\nabla}\left[q(\phi)D\vec{\nabla}U\right. \qquad (6)$$

$$\left. - \frac{w_0}{2\sqrt{2}}\left(1 + (1-k)U\right)\hat{n}\frac{\partial\phi}{\partial t}\right] + \left(\frac{1 + (1-k)U}{2}\right)\frac{\partial\phi}{\partial t}$$

where $z_{\rm int} \equiv \int_0^t V_p\, dt'$ is the interface position, $\tau(\hat{n}) = \tau_0 \cdot a^2(\hat{n})$ the relaxation time and $\hat{n} \equiv -(\vec{\nabla}\phi)/(|\vec{\nabla}\phi|)$ the unit vector normal to the interface. The interpolation function $q(\phi) = (1-\phi)/2$ governs diffusivity across the interface.

A sixfold symmetry is implemented through the anisotropy function $a(\hat{n}) \equiv a(\theta) = 1 + \epsilon_0 + \epsilon_6 cos[6(\theta - \theta_0]$, where θ is the angle between the normal to the interface and the underlying crystalline axis of the HCP structure corresponding to the $< 11\bar{2}0 >$ direction in the basal plane, and θ_0 is the angle between that crystalline axis and the direction of the thermal gradient, defining the orientation of the crystalline structure as a whole, meaning $\theta_0 = 0$ corresponds to the $< 11\bar{2}0 >$ direction of the crystal coinciding with that of the thermal-gradient. This anisotropy function is the projection in the basal plane of the spherical harmonics representing the space group of the HCP crystal lattice: $a_{3d} = 1 + \epsilon_{20}y_{20} + \epsilon_{66}y_{66}$, where ϵ_{20} and ϵ_{66} are constant coefficients weighting the contribution of each of the spherical harmonic functions $y_{20} = \sqrt{5/16\pi}[3cos^2(\Theta) - 1]$ and $y_{20} = \sqrt{6006/64\sqrt{\pi}}[sin^6(\Theta)cos(\Phi)]$ while Θ and Φ are the inclination (or elevation) and azimuth spherical coordinate angles, respectively. The applied anisotropy function has been used by Eiken et al [7] and has been validated by the experimental findings of Pettersen et al [8]

and Zhang et al [9]. From the molecular dynamics study of Sun et al ([10]) the anisotropy coefficients are given by $\epsilon_0 = 0.084$ and $\epsilon_6 = 0.03$, thus we approximate $1 + \epsilon_0 \sim 1$ and define $\epsilon_6 \equiv \epsilon = 0.03$.

In order to promote sidebranching, thermal noise induced concentration fluctuations are also included as described in [11]. Their explicit inclusion in the evolution equations is omitted here for clarity and brevity. Further details can be found at [1].

The material parameters are presented in table 1. Kinetic effects are neglected (i.e. $\beta = 0$), at least to first order, as shown in [6]. The phase-field equations are simulated using the adaptive-mesh-refinement (AMR) scheme developed by Provatas and co-workers, details of which can be found in [12, 13].

$\|m\|$ $(K/wt\%)$	5.50
c_0 $(wt\%)$	0.50
k	0.40
D $(\mu m^2/s)$	1800
Γ $(K \cdot \mu m)$	0.62
ϵ	0.03

Table 1: Material parameters defining the MgAl system. m is the liquidus slope, c_0 the alloy composition, k the partition coefficient, D the diffusivity of impurities in the liquid, Γ the Gibbs-Thomson constant and ϵ the anisotropy strength.

Two different growth conditions are simulated, on relatively small two dimensional domains, of width 1 and 2 mm. In the first case, direct thermocouple data from unidirectional solidification experiments are used to extract the local thermal gradient across the solid-liquid interface and the effective front velocity. These were then fitted to provide the functions representing $G(t)$ and $V_p(t)$. Since the pulling speed was modelled after a fit of the experimental front velocity, and the simulated interface is initially positioned at T_L, the simulated front velocity is systematically lower than the experimental front velocity used to determine the pulling speed, with the discrepancy decreasing as the system evolves. In the second case, the thermal gradient and pulling speed are kept constant. This report only presents simulations using constant growth conditions.

Results and discussions

We simulated a single grain with maximum misorientation with respect to temperature gradient under constant growth conditions of $v_p = 1$ mm/sec and $G = 2$ K/mm as shown in figure 1. These constant parameters being very close to the average transient growth conditions in our experiments. A hexagonal structure dominates at the onset, but it eventually becomes columnar. This transition can be attributed to the orientation of temperature gradient, which is selected to be different from the anisotropy direction, to be dominant. The boundary conditions at the sidewalls may also be playing a role. A detailed study of this effect, which requires simulating larger domains, is in progress. Since the thermal gradient and the surface tension compete during the whole solidification period, we can expect that a more intense thermal gradient will induce the transition earlier. To investigate the effect of temperature gradient, for the same pulling speed and initial orientation, we varied temperature gradients to $4G$, $8G$ and $16G$ as presented in figure 2 . As expected, higher temperature gradients make the transition manifest itself earlier.

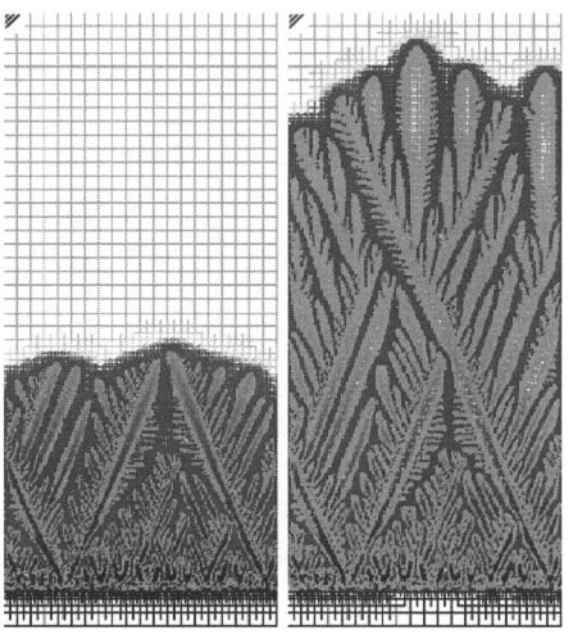

Figure 1: Single grain morphology at different stages of its evolution. The width of the simulation domain corresponds to 1 mm. Grid lines map out the structure of the adaptive mesh.

As opposed to the more commonly studied cubic structures, at the earlier stages of evolution, before the hexagonal-to-columnar transition, there can be regions

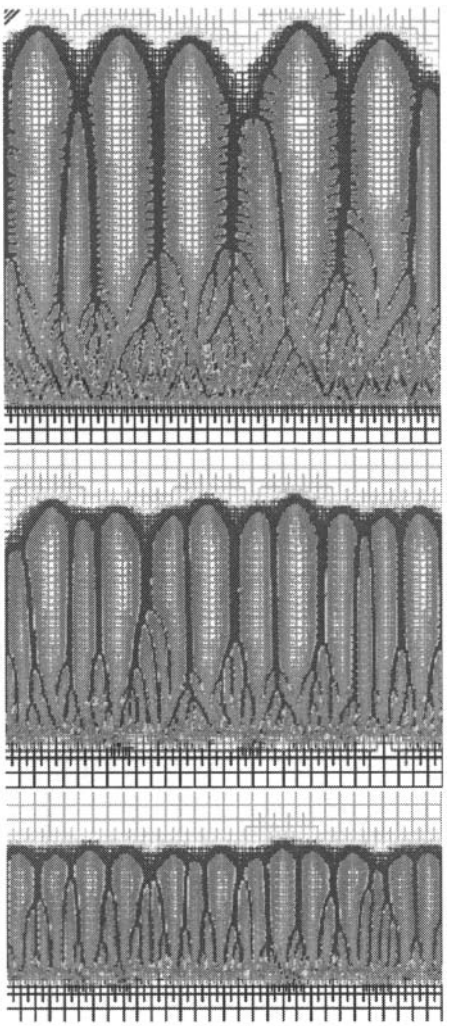

Figure 2: The hexagonal-to-columnar transition as it manifest itself earlier for more intense thermal gradient in each image, from top to bottom, increased by a factor of 4. All other parameters are the same as for figure 1.

where there is no clear distinction between primary and secondary arms. This is illustrated in the left hand frames of figure 3. The various orientations in these structures, and their relative change during hexagonal-to-columnar transitions, were analyzed here using a two-dimensional power spectral analysis algorithm developed by Kuchnio et al [14], which registers the main wavelength at different angular directions with respect to the centre of an image. The right hand frames of figure 3 show an overall shift in the distribution of orientations towards the y-directions, indicative of the columnar transition shown in the left hand frames.

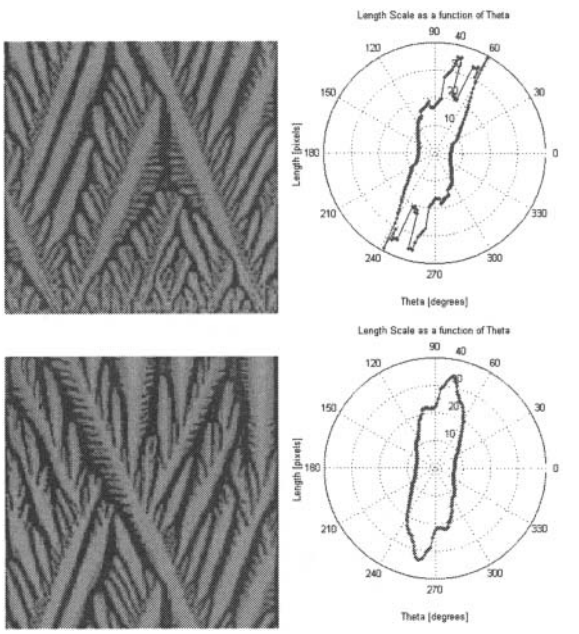

Figure 3: Main wavelength of a power-spectrum analysis performed at different angular directions with respect to the centre of a subdomain of the final structure presented in figure 1. The subdomain centred closer to the onset of the hexagonal-to-columnar transition present a closer alignment with the direction of the thermal gradient.

The hexagonal-to-columnar transition was also investigated experimentally under transient growth conditions. Growth velocity and temperature gradient are coupled in the experiments and decrease as the solidification front moves away from the chilling wall. Under these conditions, we expected to observe the transition at earlier times when the temperature gradient is highest.

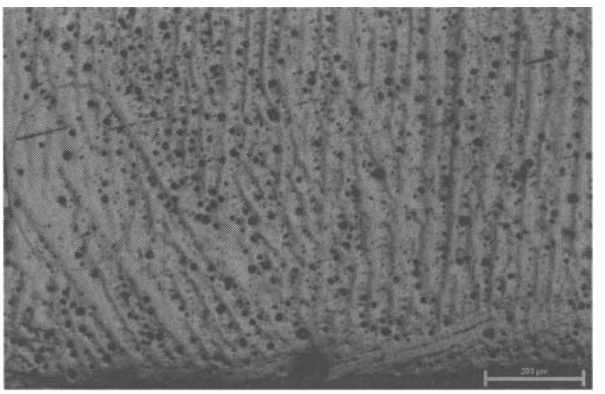

Figure 4: Different dendritic orientation showcased in a single grain obtained from a water-jet cooled sample. The red oval drawn close to the grain boundary shows the transition region from hexagonal to columnar microstructure.

However, high interface growth velocity opposes the orientation change since higher velocity means less effective time for dendrites to transition from hexagonal to columnar structure. Figure 4 shows an experimental image of a dendritic microstructure initialized from a chilling wall. Dendrites with different initial orientations exhibit both six-fold and columnar microstructure in a single grain. A hexagonal to columnar transition is observed very close to the left boundary. It is not clear to what effect this is caused by the finite size effect (i.e. due to interaction with another grain) or due to the competitive effect of thermal gradient and anisotropy, as indicated can exist from our simulations.

References

[1] Amoorezaei M., Gurevich S., Provatas N. *Spacing Characterization in Al-Cu Alloys Directionally Solidified Under Transient Growth Conditions* Acta Mater., **58**, n18, 6115-6124 (2010)

[2] Trivedi R., *Theory of dendritic growth during the directional solidification of binary alloys.*, Journal of Crystal Growth, **49**, n2, 219-32 (1980)

[3] Bouchard D. and Kirkaldy J. S., *Prediction of dendrite arm spacings in unsteady-and steady-state heat flow of unidirectionally solidified binary alloys.*, Metallurgical and Materials Transactions B, **27B**, n1, 101-13 (1996)

[4] Hunt J. D., Solidification and casting of metals, *Cellular and primary dendrite spacings.*, The metals society, London, 3 (1979)

[5] Karma A.,*Phase-field formulation for quantitative modelling of alloy solidification*, Phys. Rev. Lett. **87**, 115701/1-4 (2001)

[6] Echebarria B., Folch R., Karma A., Plapp M.,*Quantitative phase-field model of alloy solidification*, Phys. Rev. E **70**, 061604 (2004)

[7] Eiken J., *Dendritic growth texture evolution in Mg-based alloys investigated by phase-field simulation.*, Int. J. of Cast Materials Research,**22**, 1-4 (2009)

[8] Pettersen K., Lohne O., Ryum N., *Dendritic solidification of magnesium alloy AZ91.*, Mettal. Trans. A.,**21A**, 221-230 (1990)

[9] Zhang C., Ma D., Wu K.-S., Cao H.-B., Cao G.-P., Kou S., Chang Y. A., Yan X.-Y., *Microstructure and microsegregation in directionally solidified Mg-4Al alloy.*, Mettal. Trans. A.,**21A**, 221-230 (2007)

[10] *Crystal-melt interfacial free energies in hcp metals: A molecular dynamics study of Mg* D. Y. Sun, M. I. Mendelev, C. A. Becker, K. Kudin, T. Haxhimali, M. Asta, J. Hoyt, A. Karma and D. J. Srolovitz: Phy. Rev. B, **73**, 024116 (2006)

[11] Echebarria B., Karma A., Gurevich S. *Onset of sidebranching in directional solidification.*, Phys. Rev. E **81**, 021608 (2010)

[12] Provatas N., Goldenfeld N., Dantzig J.,*Efficient computation of dendritic microstructures using adaptive mesh refinement.*,Phys. Rev. Lett. **80**, n15, 3308 (1998)

[13] Athreya B. P., Goldenfeld N., Dantzig J. A., Greenwood M., Provatas N., *Adaptive mesh computation of polycrystalline pattern formation using a renormalization-group reduction of the phase-field crystal model.*, Phys. Rev. E,**76**, n5, 056706/1-14 (2007)

[14] Kuchnio P., Tetervak A., Watt C., Henein H., Provatas N., *Quantification of rapidly solidified micrpstructure of Al-Fe droplets using correlation length analysis.*, Metalurgical and Materials transactions A, **40**, n1, 196-203 (2009)